A COUPLED NUMERICAL/EXPERIMENTAL STUDY OF FLOW SEPARATION SUPPRESSION OVER A CURVED SURFACE USING FLUIDIC OSCILLATORS

Nicholson K. Koukpaizan PhD candidate
Curtis J. Peterson PhD candidate
Ari Glezer Professor
Marilyn J. Smith Professor
Georgia Institute of Technology
Atlanta, Georgia, USA

ABSTRACT

Fluidic oscillators, devices that generate sweeping jets when supplied with a pressurized fluid, have been used in a variety of flow control applications. The present investigations focus on understanding the physics and numerical prediction of these devices to control separation over a curved surface appropriate for rotorcraft applications. High-fidelity simulations and experimental data are employed to identify the mechanisms responsible for the control of separation. The model design includes an overhang at the interface between the actuators and the outer flow. At this interface, small scale spanwise vortices are shed in the streamwise direction, thereby enhancing wall-normal mixing. The spatial evolution of the sweeping jets give rise to large-scale structures between them causing spanwise mixing. In the mean sense, the jets lead to the formation of recirculation regions near the actuator exits inducing a deflection of the outer flow towards the wall. The simulations also examine the effects of fully resolving the interior of the oscillators, or using a boundary condition model, including turbulence. This boundary condition was found to be able to reproduce the correct physics of the flow control application, including mixing of the sweeping jets with the outer flow.

NOTATION

$\tilde{a}$	Speed of sound (m/s)
$\tilde{A}$	Area (m^2)
$\tilde{c}$	Chord length (m)
C_μ	Jet momentum coefficient, $\frac{\tilde{T}hrust_{jet}}{\tilde{\rho}_\infty \tilde{U}_\infty^2 \tilde{A}_{ref}}$
$\tilde{c}_v$	Specific heat at constant volume (J/(Kg.K))
$\tilde{E}$	Stagnation energy, $\tilde{c}_v\tilde{T}+\tilde{U}^2/2$ (m^2/s^2)
$\tilde{H}$	Depth of the fluidic oscillator (m)
$\tilde{k}$	Turbulent Kinetic Energy (m^2/s^2)
$\tilde{L}$	Length (m)
M	Mach number, $\tilde{U}/\tilde{a}$
$\tilde{p}$	Static pressure (Pa)
$\tilde{q}$	Dynamic pressure, $0.5\tilde{\rho}\tilde{U}^2$ (Pa)
$\tilde{Q}$	Q criterion, $\left(\tilde{R}_{ij}\tilde{R}_{ij}-\tilde{S}_{ij}\tilde{S}_{ij}\right)/2$ (1/s^2)
Re	Reynolds number, $\tilde{U}\tilde{L}/\tilde{\nu}$
$\tilde{R}_{ij}$	Symmetric velocity gradient tensor, $(\partial\tilde{u}_i/\partial x_j+/\partial\tilde{u}_j/\partial x_i)/2$ (1/s)
$\tilde{S}_{ij}$	Antisymmetric velocity gradient tensor, $(\partial\tilde{u}_i/\partial x_j-\partial\tilde{u}_j/\partial x_i)/2$ (1/s)
$\tilde{t}$	Physical time (s)
$\tilde{T}$	Static temperature (K)
$\tilde{\overline{T}}$	Period (s)
$\tilde{u},\tilde{v},\tilde{w}$	Velocity components in the x, y, z, directions respectively (m/s)
$\tilde{u}_\tau$	Friction velocity, $\sqrt{\tilde{\tau}_w/\tilde{\rho}}$ (m/s)
$\tilde{U}$	Velocity magnitude (m/s)
$\tilde{W}$	Width at the throat of the fluidic oscillator (m)
y^+	Wall unit normalized wall distance, $\tilde{y}\tilde{u}_\tau/\tilde{\nu}$
$\Delta\tilde{t}$	Physical time step (s)
$\tilde{\nu}$	Kinematic viscosity (m^2/s)
$\tilde{\omega}$	Specific dissipation rate (1/s)
ϕ	Phase (rad)
$\tilde{\rho}$	Density (Kg/m^3)
$\tilde{\tau}_w$	Wall shear stress (Pa)
$\overline{(\,)}$	Time average $\frac{1}{\tilde{T}}\int_0^{\tilde{T}}(\,)dt$
$\tilde{(\,)}$	Dimensional quantity
$(\,)_\infty$, $(\,)_0$	Freestream
$(\,)_{ref}$	Reference

1 INTRODUCTION

The need for improved performance, reduced drag and more energy efficient rotary-wing vehicles has motivated the aerospace community to design, investigate, and implement various flow control techniques. To meet future design goals for rotorcraft,

Presented at the 45th European Rotorcraft Forum, Warsaw, Poland, September 17-20, 2019.

various sources of performance loss such as fuselage drag in forward flight (on the order of 30% of the total helicopter drag[1]) and rotor download in hover must be mitigated. Active Flow Control (AFC) is one of the few technologies that shows promise to achieve significant drag and download reduction. The global effectiveness of these techniques has been demonstrated in multiple scaled experiments, but the fundamental physics leading to the overall control is not fully understood. One such technique is active separation control via fluidic oscillators[2]–[6].

A fluidic oscillator, also known as a sweeping jet actuator, is a device without any moving parts that generates a sweeping jet when supplied with pressurized fluid. These actuators are naturally unstable and capable of producing large disturbances to influence other flows with minimal input. The most common fluidic oscillators can be classified in two categories: bi-stable or wall-attachment (single or double feedback loop) and feedback-free (or jet interaction). The sweeping motion of these jets results in a larger impacted area (as compared to a steady blowing jet), which allows their implementation to contain fewer or smaller devices positioned further apart while maintaining the same or larger impacted area. Research indicates that control of flow separation using sweeping jets is achieved not only by adding momentum directly to the boundary layer, but also by manipulating the vortical structure of the outer crossflow, thereby increasing turbulent mixing. Otto et al.[7] experimentally demonstrated the superiority of sweeping jets, as compared to steady jets, to control the separation over the NASA wall-mounted hump. This was attributed to the presence of more coherent streamwise vortices formed due to the fluidic oscillators, a behavior that was also observed by other researchers[8],[9] during the interaction of sweeping jets with a crossflow over a flat plate.

Martin et al.[5] observed a drag reduction on the order of 20% in their wind-tunnel experiments on the NASA Robin-Mod7 fuselage with fluidic oscillators embedded in the fuselage ramp. Yadlin et al.[6] reported a 30% reduction in download by employing fluidic oscillators on a V-22 tilt-rotor during hover. Reviews of active flow control techniques and the development and application of fluidic oscillators for flow control are provided by Raghu[10], Cattafesta and Sheplak[11], and Gregory and Tomac[12].

Shmilovich and Vatsa[13] recently proposed a review of practical computational techniques that they have employed for flow control applications. The URANS (Unsteady Reynolds-Averaged Navier-Stokes) and Lattice-Boltzmann (with Very Large-Eddy Simulation) approaches were reported to efficiently provide engineering accuracy at realistic computational costs. The reported computational cost (URANS) was approximately 30,000 CPU hours for actuators with an oscillation frequency of 225 Hz integrated into a Boeing 757 vertical tail. The computational cost is expected to increase with the oscillation frequency.

HRLES (Hybrid RANS/Large-Eddy Simulation) techniques have also been applied in conjunction with the Navier-Stokes equations[14]–[16]. The simulations of Aram et al.[15] indicated a superiority of IDDES (Improved Delayed Detached-Eddy Simulation) over URANS in predicting the behavior (jet penetration, spreading and angle) of a sweeping jet emanating from a double feedback loop actuator into a quiescent field. Koukpaizan et al.[16] also showed improvements of their predictions with HRLES and DDES for a sweeping jet generated by a jet-interaction fluidic oscillator, though not to the extent demonstrated by Aram et al. While Aram et al. observed differences on the order of 40% for the sweeping jet velocity profiles between URANS and IDDES, Koukpaizan et al. only observed differences on the order of 10%. The oscillation frequencies simulated in these two cases differ by three orders of magnitude. In both cases however, performing the simulation in three dimensions (3D) was found to be crucial.

In the presence of multiple actuators, two computational approaches are generally adopted. The first consists in resolving flow internal to all actuators simultaneously with the external flow[17],[18]. This poses challenges with respect to the computational cost, not only in terms of the grid size, but also in terms of the time scale difference between the flow internal to the actuators and the base flow. In a second approach, a boundary condition (BC) derived from the simulation of a single isolated actuator in quiescent conditions is applied at the throat of the distributed devices[14],[19]. Koukpaizan et al.[16] recently evaluated, in quiescent conditions, a number of boundary conditions applied at the throat or exit of the devices. They also assessed the importance of the modeled and resolved turbulence in the boundary condition formulation. A boundary condition based on a phase-averaged representation of the the flow variables applied at the throat of the fluidic oscillator provided an accuracy comparable to the fully resolved cavity simulation, and the differences observed were attributed to the lower levels of resolved turbulence present in the phase-averaged representation. The boundary condition was found to be more sensitive to turbulence at the actuator exit, and this sensitivity is likely to increase further downstream in the jet. The drawback of any boundary condition model is that, unless general scaling relations are known, the isolated actuator must be simulated for each driving pressure or flow rate considered in the flow control application.

For the present paper, the control of flow separation over a curved surface was simulated and compared with experiments. Simulations were conducted either by resolving the interior of the actuators or using

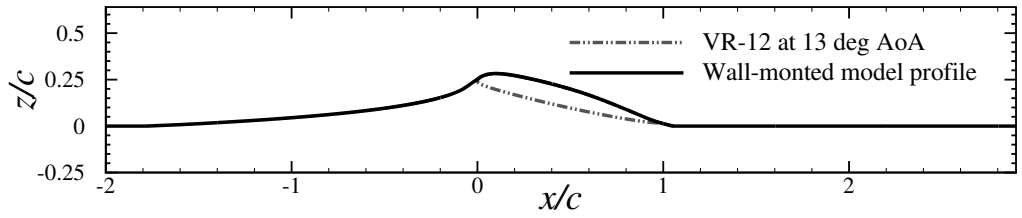

Fig. 1: Wall-mounted wind tunnel model profile

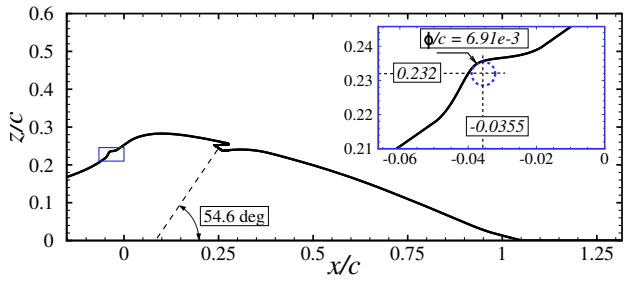

Fig. 2: Modified surface shape to mimic the presence of a trip wire

a boundary condition model. The fluidic oscillators were also simulated in quiescent conditions to characterize their response to inlet pressure and derive the boundary condition model. No claim is made regarding the efficiency of the setup employed to suppress the separation over the wind tunnel model; the focus is rather placed on understanding the physics involved, in particular the role of turbulence and jet interactions, and evaluating the ability of numerical methods to resolve these physics.

2 METHODOLOGY

A wall-mounted wind tunnel model integrating a spanwise array of seventeen jet interaction fluidic oscillators has been designed based on the VR-12 airfoil shape, as depicted in Fig. 1. This geometry was selected to reflect the type of separated flows that would be observed at the back of a helicopter fuselage or over a rotor blade at a high angle of attack. The model has been designed to study in detail the turbulence and jet interactions of an array of fluidic oscillators through simulation and experiments. The wall-mounted model has chord $\tilde{c} = 62.23$ mm (2.45 in). To further promote flow separation, a trip wire of diameter 0.43 mm (0.0169 in) was glued to the physical model at x/c = -0.0355 and was represented in the simulations as illustrated in Fig. 2. The spanwise oscillating actuators are oriented approximately 54.6° with respect to the horizontal axis due to spatial constraints and are spaced by 7 mm (0.276 in). Figure 3 illustrates the key features of the jet interaction fluidic oscillator. Two supply jets interact and give rise to recirculation regions in the dome, upper and lower

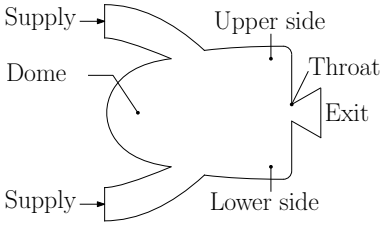

Fig. 3: Feedback-free or jet interaction fluidic oscillator

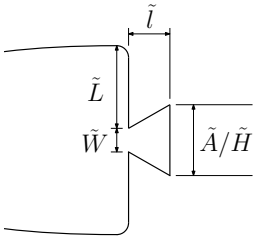

Fig. 4: Definition of the key dimensions of the fluidic oscillator

sides. The upper and lower side vortical structures emerge and dissipate periodically, concomitant with a deflection and bifurcation of the supply jets, leading to a spatial oscillation of the jet emanating from the actuators' throat[16],[20].

Figure 4 summarizes the definition of the jet interaction fluidic oscillator dimensions. In the present work, the inner orifice (or throat) is normal to actuator's internal cavity centerline and has a width $\tilde{W} = 0.5$ mm (0.0197 in). The internal height of the actuator cavity normal to the plane of oscillations is $\tilde{H} = 1$ mm (0.0394 in). The outer orifice (or exit) has a width $\tilde{A}/\tilde{H} = 1.24$ mm (0.0488 in), where $\tilde{A}$ is its area. The nozzle has length $\tilde{l} = 1$ mm and the distance from the cavity side to the throat is $\tilde{L} = 1.58$ mm (0.0622 in).

2.1 Experimental Setup

Experiments were conducted to study the flow over the model within a wind tunnel, as well as to characterize the fluidic oscillators outside of the test geometry in quiescent conditions. The wind tunnel test section length, width, and height are $\tilde{L} = 660.4$ mm (26 in) and $\tilde{W} = \tilde{H} = 127$ mm (5 in) respectively. With a nominal Mach number of 0.25, the Reynolds

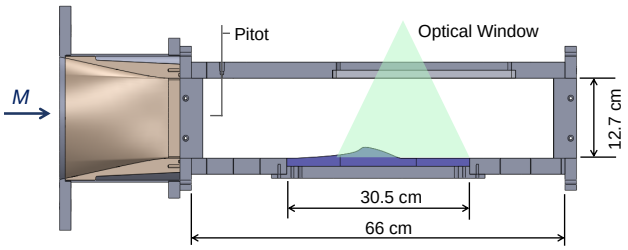

Fig. 5: Wall-mounted model in the wind-tunnel test section

number based on the chord length is approximately 345,000. Wind tunnel experiments were conducted at the Fluid Mechanics Research Laboratory at Georgia Tech, and initial measurements of the centerline pressure and mid-plane PIV (Particle Image Velocimetry) data were reported by Peterson et al.[21].

PIV measurements were done in multiple, partially-overlapping fields of view along the central plane, which were then integrated together to create composite flowfields. This process maintains fine spatial resolution across the entire measurement domain. Each set of PIV measurements was taken at 200 Hz and ensemble averages were based on over 1,000 image pairs. Furthermore, the total and static pressure ports at the test section inlet were measured by two *baratron* pressure transducers and sampled by a DAQ (Data Acquisition) computer. The central symmetry plane of the model also contains a number of static surface pressure ports measured by a dedicated *PSI* Netscanner system. Each set of those measurements was based on sixty-four independent samples, while the mean static and total pressures were based on seventy-five data sets.

The oscillation frequency of the fluidic oscillators was estimated from hot-wire measurements at the centerline of the sweeping jet, at a distance $0.05c$ normal to the actuator exit. A model of the fluidic oscillators is mounted in a plenum that issues into quiescent air for such bench top measurements. The hot-wire probe is situated perpendicular to the oscillation direction of the jet, and measurements are sampled at 46 kHz with a final frequency resolution of 1Hz.

The wind tunnel experiments confirmed the ability to asymptotically suppress separation over the model with increasing momentum coefficient (C_μ). The results also suggest an entrainment of the outer flow by the sweeping jets resulting in the downward vectoring of the separated shear layer towards the curved surface causing flow reattachment.

2.2 Flow Solver

The numerical evaluations were carried out using an in-house state of the art CFD solver, GTsim, initially developed and validated by Hodara[22]. The code is finite-volume (cell-centered) and operates on block-structured grid topologies to achieve high efficiency and numerical accuracy. Second-order, fourth-order, and fifth-order spatial discretization schemes are implemented, as well as a second-order temporal discretization (Backward Differentiation Formula). Dual-time stepping is used to ensure time-accuracy. Turbulence equations are loosely coupled to the Navier-Stokes equations for a range of closures including URANS, LES (Large Eddy Simulation), HRLES (Hybrid RANS-LES) with a subgrid-scale (SGS) model, the family of Detached Eddy Simulation (DES) models, and very large DNS (Direct Numerical Simulation). Laminar to turbulent transition is modeled with the Langtry-Menter $\gamma - Re_\theta$ model[23] and the tHRLES (transitional HRLES) of Hodara[24].

In the present effort, the URANS approach employed is the $k-\omega$ SST model of Menter[25]. For the advanced turbulence closure analyses, the HRLES closure is that of Sánchez-Rocha[26], which blends the $k-\omega$ SST model and the Localized Dynamic Kinetic-Energy Model (LDKM) of Kim[27]. Here, the HRLES model coefficients were kept constant, and the cross-coupling hybrid terms were not included. The hybrid terms were designed to permit the transfer of momentum in the RTLT (RANS To LES Transition) region, but were found to be unstable for massively separated flow over periodic hills[22]. The fourth-order central difference scheme was adopted to simulate the baseline flow, while the Roe scheme[28] was adopted with a direction-by-direction fifth-order WENO (Weighted Essentially Non-Oscillatory) reconstruction[29] in the presence of the sweeping jets. In the latter configuration, supersonic conditions are reached within the computational domain, therefore requiring a shock-capturing scheme. Though the direction-by-direction WENO reconstruction in a finite-volume code formally remains second-order accurate for three-dimensional non-linear fluxes, improvements are still visible compared to a MUSCL (Monotone Upstream-Centered Schemes for Conservation Laws) reconstruction, in particular for turbulent flows[30]. For improved robustness, the code reverts to MUSCL when WENO results in negative density or temperature, which can occur at boundaries and locations where multiple discontinuities are in close proximity[31].

3 BASE FLOW CHARACTERIZATION

The base (non-blowing) flow over the wall-mounted model was evaluated using the URANS approach. The results herein were obtained on the grid depicted in Fig. 6. The complete three-dimensional grid contains 42.8 million cells, including 7 million cells for the actuators, 1.6 million cells for the domain between the actuators' exits and the surface of the model, and 34.2 million cells for the wind tunnel section. The

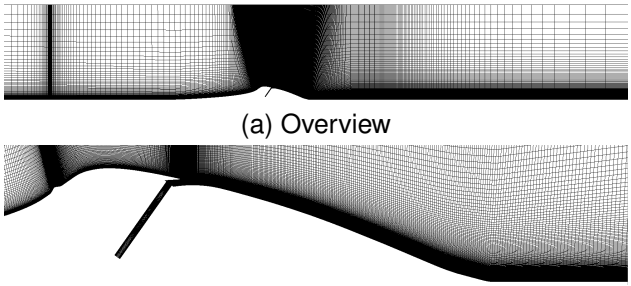

(a) Overview

(b) Close view of the curved surface

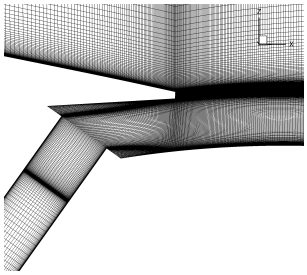

(c) Close view of the actuator exit

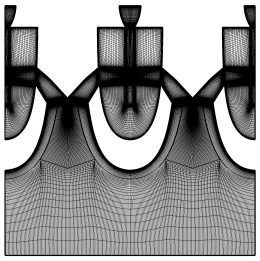

(d) Close view of the fluidic oscillators

Fig. 6: Grid system including the curved surface and the fluidic oscillators

size of the latter domain is driven by the relatively large number of cells (194) in the spanwise direction over approximately 0.2 chords. The actuator domains were disregarded during the base flow characterization. The wall spacing y^+ was verified to be less than 1 everywhere in the domain. Subsonic inflow conditions were applied at the left boundary of the wind tunnel, and a back pressure was specified at the right boundary. The upper boundary of the wind tunnel was modeled as a slip wall to reduce the computational cost. While characterizing the base flow, a simulation was performed in two dimensions (2D) with a viscous wall instead of a slip wall, resulting in a better recovery of the pressure coefficient upstream of separation, but without significant change to the predictions in the separation region.

The resulting pressure distribution is compared to experiments in Fig. 7, where the reference pressure is taken as the pressure far downstream of the model. Figures 8 and 9 provide comparisons between computation and experiments of the time-averaged vorticity and Turbulent Kinetic Energy (TKE or k) respectively. Here, the simulation TKE is entirely modeled with URANS. The base flow separates early over the curved surface (30% chord), and the separated flow exhibits regions of large vorticity and TKE. The vorticity and TKE exhibit similar levels in the mid-plane flowfield. The relative error between computation and experiment is between 1% and 7% for the pressure distribution away from the separation and reattachment locations ($0.5 < x/c < 1.2$). The computational predictions are satisfactory considering the uncertainty on the shape of the trip wire, and the characteristics

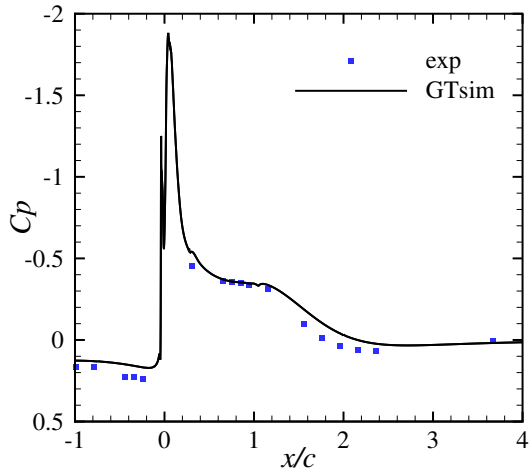

Fig. 7: Base flow pressure coefficient distribution over the curved surface

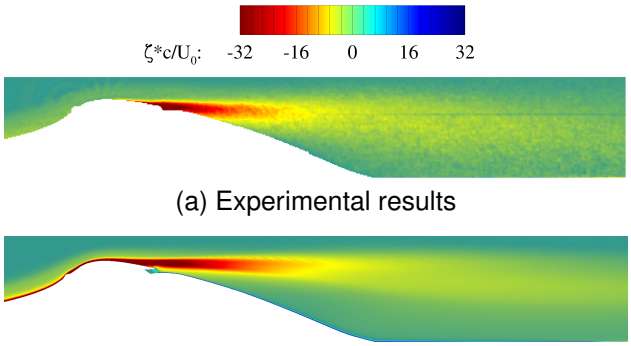

(a) Experimental results

(b) Present simulation

Fig. 8: Base flow mean out-of plane vorticity contours

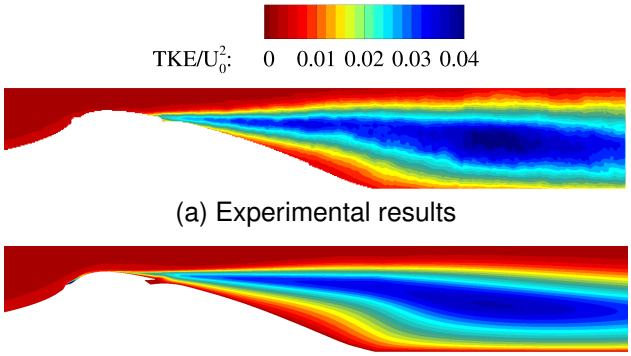

(a) Experimental results

(b) Present simulation

Fig. 9: Base flow mean in-plane TKE ($\overline{u'^2 + w'^2}/2$) contours

of the incoming boundary layer. Attempts to improve this solution by using advanced turbulence closures have been unsuccessful so far.

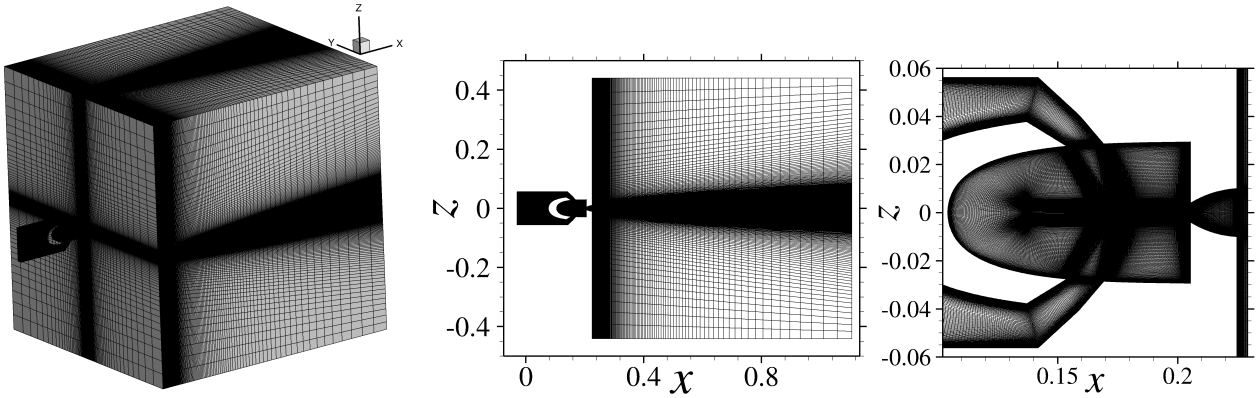

(a) Overview of 3D the grid (b) Overview of the mid-plane (c) Close view of the cavity

Fig. 10: Grid employed to characterize the isolated fluidic oscillator in quiescent conditions

4 FLUIDIC OSCILLATORS IN QUIESCENT CONDITIONS

The flow solver GTsim was evaluated with success through simulations of an isolated fluidic oscillator in quiescent conditions in previous studies[16]. These studies revealed the requirement for time accuracy throughout the entire simulation, as well as the necessity to perform the simulations on three-dimensional domains to capture the dual-peak in the sweeping jet velocity distributions[16]. Across all simulations performed, the oscillation frequency remained within 5% of the experimental value of 12.6 kHz for a supply pressure ratio of 2.45.

An approach similar to that detailed in Ref. [16] was adopted for the actuator design implemented in the wall-mounted model to characterize the oscillation frequency and develop adequate boundary conditions for the flow control application. More specifically, time-accurate simulations were performed in three dimensions, with the HRLES turbulence closure and a fifth-order WENO reconstruction. Grid and time-step refinement studies were not repeated here. Multiple supply pressures were considered in both the computations and experiments. In addition, a simulation was performed with two oscillators in quiescent conditions to assess their interactions in the absence of a crossflow.

4.1 Single sweeping jet in quiescent conditions

A single isolated sweeping jet was evaluated in quiescent conditions. Figure 10 illustrates the computational grid. It contains approximately 33.9 million cells, half of which are in the quiescent field. While this level of resolution is not necessary to resolve the fluidic oscillators, it was required to characterize the sweeping jet with HRLES. Furthermore, this relatively fine grid permitted the collection of high-quality data

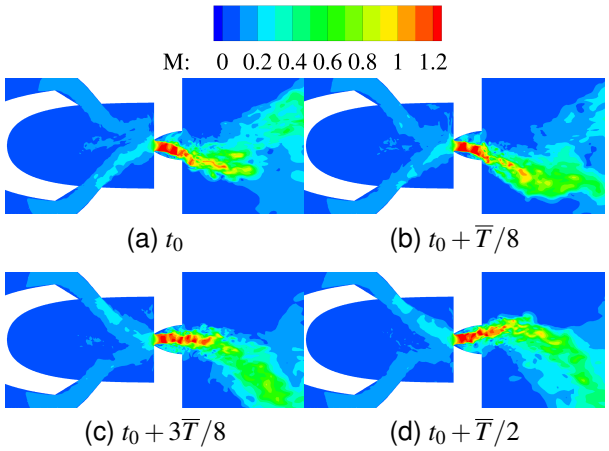

(a) t_0 (b) $t_0 + \overline{T}/8$

(c) $t_0 + 3\overline{T}/8$ (d) $t_0 + \overline{T}/2$

Fig. 11: Instantaneous local Mach number contours at the mid-plane over a half-period of oscillation, 2.0 pressure ratio

for the boundary condition models, which could be interpolated onto coarser grids if needed. The wall spacing y^+ was verified to be less than 1 everywhere in the domain. The physical time step was selected to obtain at least 1000 iterations per oscillation cycle at the highest pressure ratio examined.

Two pressure ratios were evaluated: 1.3 and 2.0. Figures 11, 12 and 13 illustrate the flowfield obtained from these simulations for a pressure ratio of 2.0. A half cycle of oscillation is depicted in Fig. 11. Concomitant with the sweeping motion of the jet into the quiescent field, the deflection of the supply jets by the upper and lower side vortices can be observed. More detailed discussions of the internal flow dynamics are given in Ref. [16] and [20]. The iso-surfaces of Q-criterion (Fig. 12) confirm that most of the turbulent scales are resolved rather than modeled due to the relatively fine grid, the fifth-order WENO scheme and the turbulence closure. The flow structures visible at the edge of the sweeping jet are indicative of mixing with the quiescent environment. Finally, the

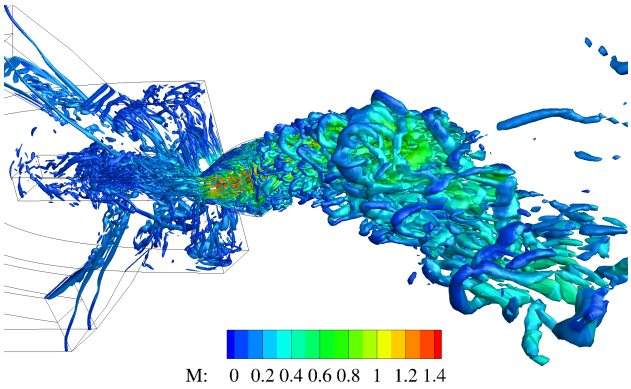

Fig. 12: Iso-surfaces of the second invariant of the velocity gradient tensor ($Q = 2000$) colored with values of local Mach number for a single isolated fluidic oscillator in quiescent conditions, 2.0 pressure ratio

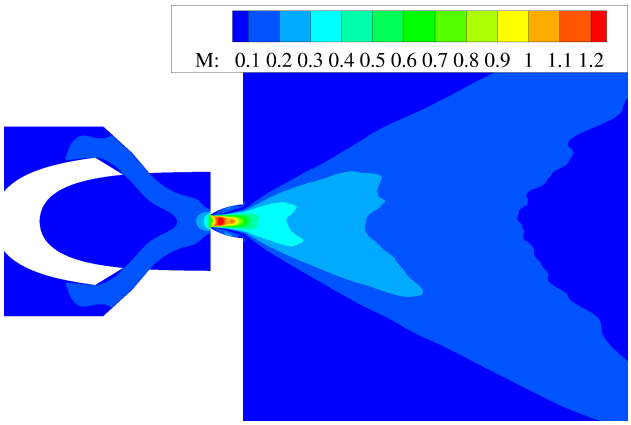

Fig. 13: Time-averaged (10 cycles) Mach number contours for a single isolated fluidic oscillator in quiescent conditions, 2.0 pressure ratio

time-averaged flow (Fig. 13) exhibits a dual peak in the Mach number contours, characteristic of sweeping jets.

Figure 14 is a comparison between the simulated frequencies and the hot wire measurements. The oscillation frequency is overestimated by the simulations. A surprising observation is that there is a significant difference between the 2D URANS and 3D HRLES estimates. The 2D URANS solution is in better agreement with the experiments with a 12% relative error, whereas the error is 20% with 3D HRLES. In previous studies of Koukpaizan et al.[16] on a different actuator size, the frequency was found to vary by less than 5% between 2D URANS and 3D HRLES. Experimentally, the present pressure measurements were obtained from a large plenum upstream of the actuator array. The working hypothesis is that there are pressure losses between that location and the computational inlet plane. Further investigation is left as future work.

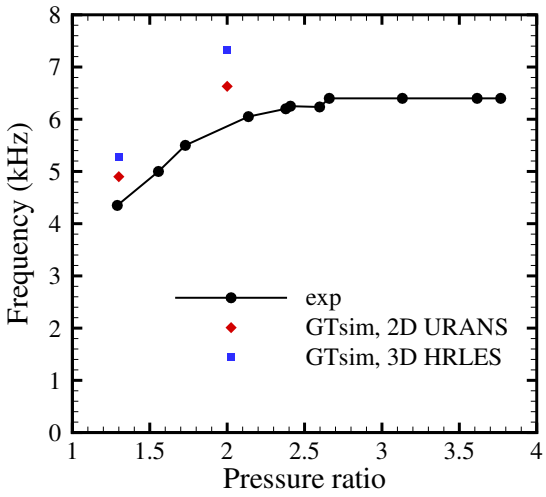

Fig. 14: Sweeping jet frequency response at different pressure ratios

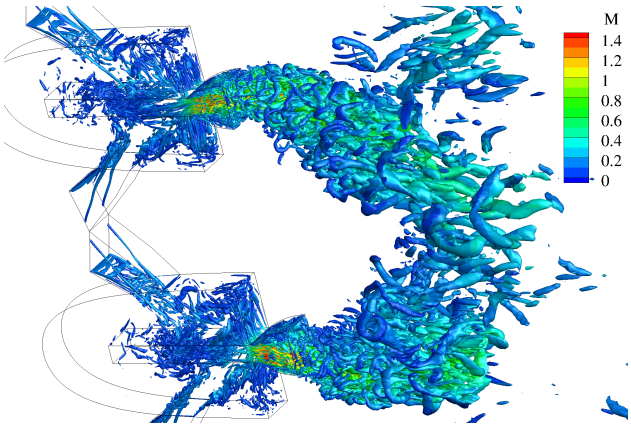

Fig. 15: Iso-surfaces of the second invariant of the velocity gradient tensor ($Q = 2000$) colored with values of local Mach number for two isolated fluidic oscillator in quiescent conditions, 2.0 pressure ratio

4.2 Two Sweeping Jets in Quiescent Conditions

Two adjacent sweeping jets were examined numerically in quiescent conditions to gain some insight into their interaction for the given spacing. A similar study was conducted experimentally by Hirsch and Gharib[32] using Schlieren visualization. Their results indicated that the sweeping jet actuators do not interact with one another, in the sense that their oscillation frequency does not vary in the presence of neighboring actuators. This behavior was observed to be independent of their separation distance. This does not mean that the ensuing sweeping jets do not interact with one another. In the present work, the separation distance is fixed and the interactions are considered both from internal and external perspectives.

The grid contains approximately 72.4 million cells, a third of which are in the quiescent field. The actuators' grid domains are identical to the ones used for the single actuator simulation.

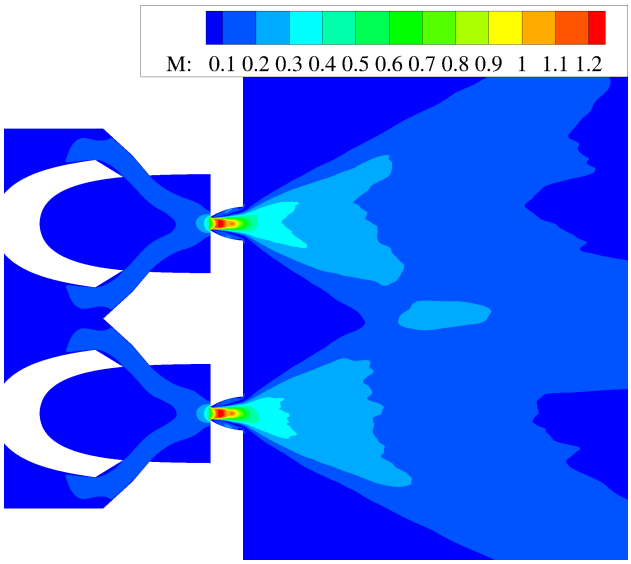

Fig. 16: Time-averaged (9 cycles) Mach number contours for two isolated fluidic oscillators in quiescent conditions, 2.0 pressure ratio

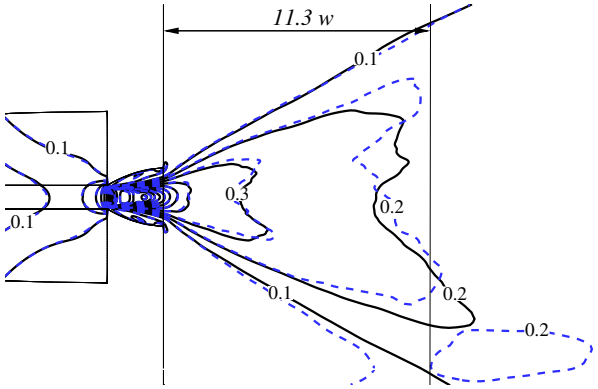

Fig. 17: Comparison of the time-averaged Mach number contour lines between one (solid black lines) and two fluidic oscillators (dashed blue lines) in quiescent conditions, 2.0 pressure ratio.

Figures 15 and 16 illustrate the flowfield obtained from these computations. Similar to the single isolated oscillator, the time-averaged flowfield exhibits a dual peak in the Mach numbers for each actuator in the present configuration. New features are created by the interaction of the two neighboring sweeping jets. This is more clearly observed by comparing the time-averaged flowfield between the simulations of a single actuator and two actuators (Fig. 17). The upper actuator was chosen for comparison in the case of two actuators. The contour lines are superimposed inside the actuator up to its exit. These interior contours overlap for both cases, which shows that the interactions only result in differences outside of the oscillator exits. This further suggests that, deriving a boundary condition based on a single actuator and extending it to an array is a valid approach. A new contour line (Mach level 0.2) appears approximately 11 throat widths downstream of the actuator exit, indicating a merging of the two sweeping jets, due to their spreading, at that location. This can also be observed in the instantaneous iso-surfaces of Q-criterion (Fig. 15). The oscillation frequency of each jet was found to be unaffected by the presence of the other jet. This is consistent with the experiments, as the oscillation frequency did not vary from testing an array of actuators to testing a single actuator (by blocking the exit of the other actuators in the array).

4.3 Boundary Condition Model Development

A boundary condition model was developed based on the behavior of the single isolated oscillator in quiescent conditions. The approach retained consists in a phase-averaged representation of the flow variables, including the modeled turbulence: the density ρ, momenta (ρu, ρv, ρw), stagnation energy E, TKE and specific dissipation rate ω. The variables were recorded at the throat of the device at every iteration of the precursor simulation. Phase-averaging was applied, with a window of 1°, in order to generate data at 100 phases between 0 and 2π rad, while retaining some of the resolved turbulent scales. The phase-averaged data were then interpolated onto the coarser grid of the actuator throat employed to simulate the control of flow separation. In deriving the boundary condition model, the momentum vector from the precursor simulation was rotated by 54.6° to match the actuator orientation in the flow control grid. The next section discusses the application of this boundary condition to examine the control of flow separation over the curved surface.

5 CONTROL OF FLOW SEPARATION

The control of flow separation over the wind-tunnel model via an array of fluidic oscillators is now investigated. Numerical simulations were performed for the maximum actuation case experimentally tested corresponding to a jet momentum coefficient $C_\mu \times 10^3 = 2.1$. According to the experimental calibration in quiescent conditions, this flow rate is achieved with a driving pressure ratio approximately equal to 2.0. There is an uncertainty regarding the validity of the calibration for wind on conditions, as the pressure over the model is lower than that in quiescent conditions. Until this can be further assessed, this information was used as a boundary condition for the numerical study.

Two fluidic oscillators were numerically modeled for comparison with the associated wind tunnel test section. Periodic boundary conditions were applied to the spanwise boundaries to generate an infinite array of actuators. An overview of the computational grid is presented in Fig. 6; part of the grid was utilized to

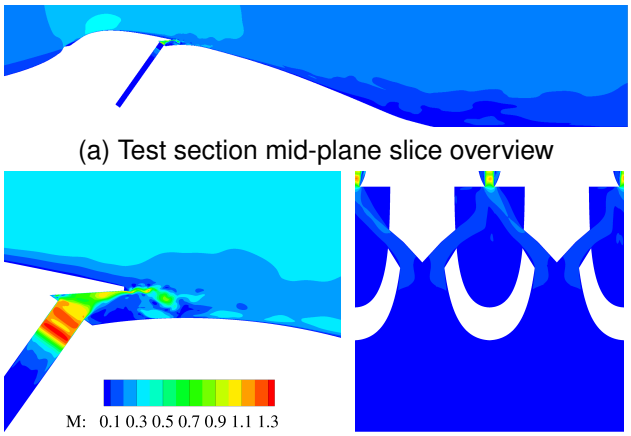

(a) Test section mid-plane slice overview

(b) Close view of the actuator exit

(c) Actuator interior

Fig. 18: Instantaneous Mach number contours for the simulation of the curved surface and two fluidic oscillators, full cavity HRLES

simulate the base flow. The computations of the controlled cases were carried out by two separate methods and compared: either by resolving the interior of the fluidic oscillators or via the new boundary condition model. In the latter case, the two devices are considered in phase, whereas the phase was a natural outcome from resolving the interior of the devices. While resolving the full cavity, the computational physical time step was set to capture 500 iterations per cycle. Since there is less restriction on time step with the boundary condition model, this time step was increased to perform 1000 iterations per chord in the outer flow at the nominal Mach number, corresponding to 165 iterations per cycle approximately. The numerical solution was averaged over more than 30 cycles of sweeping jet oscillations. Both the URANS and HRLES approaches were evaluated.

The computations are compared to time-averaged PIV measurements in the test section center plane and pressure measurement along the model centerline. The computations can provide further insight into the physics, such as the flow behavior close to the actuator exits where cameras have no access. Figure 18 is a snapshot of the instantaneous Mach number contours in the spanwise mid-plane of the actuators and test section. The sweeping jets impinge on the overhang, from which small scale vortices are shed into the outer flow. The spanwise oscillation of the jets allow this shedding to occur over a wider area. Figure 19 depicts the iso-surfaces of Q-criterion for the full cavity solution. Both the URANS and HRLES results are depicted. The locations of the actuators are identified by black triangles in Fig. 19. Of course, fewer scales are resolved with the URANS approach. Large-scale structures are formed between the sweeping jets, and result in stripes convecting downstream. This is observed more clearly in

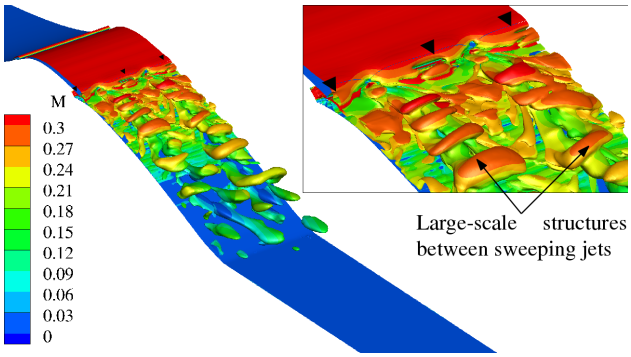

(a) Full cavity URANS

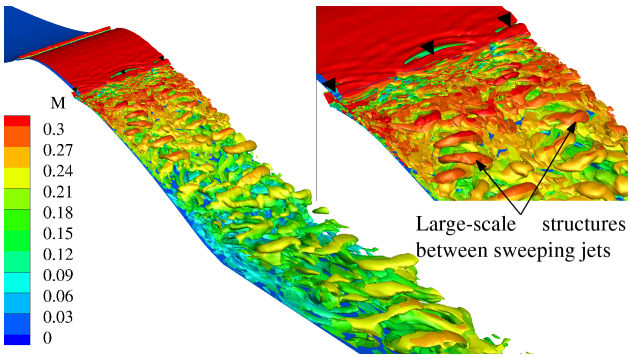

(b) Full cavity HRLES

Fig. 19: Iso-surfaces of the second invariant of the velocity gradient tensor ($Q = 1$) colored with values of local Mach number for the controlled flow over the wind-tunnel model

the URANS figure, as the smaller scales are not resolved. Indicative of attached flow, the flow structures are much smaller in the regions directly impacted by the sweeping jets. Similar structures were observed with the boundary condition models.

Figure 20 is the pressure coefficient at the centerline of the model. Once again, the pressure offset upstream of the model is a result of neglecting the wind-tunnel top and side walls in the computational setup. The pressure distributions indicate that the simulations are able to correctly predict the suppression of separation. This is further supported by the streamlines of the mean flow depicted in Fig. 21. The formation of vortices near the actuator exits is also apparent in the latter figure. These vortices correspond to the spikes (around $x/c = 0.3$) in the pressure distribution plotted in Fig. 20. According to the pressure coefficient distribution, the most accurate agreement with experimental data is obtained with the boundary condition model and the URANS closure. The maximum discrepancy between the simulation approaches and the experiments when comparing the pressure coefficients occurs at the trailing edge ($x/c \simeq 1$). Around this location, the different simulation approaches have up to 100% relative error when compared to one another, whereas they are within 10% of one another in location of non-zero pressure coefficient and away

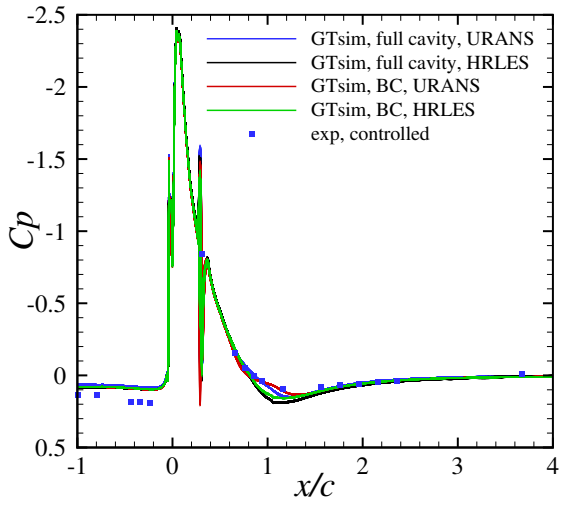

(a) Overview

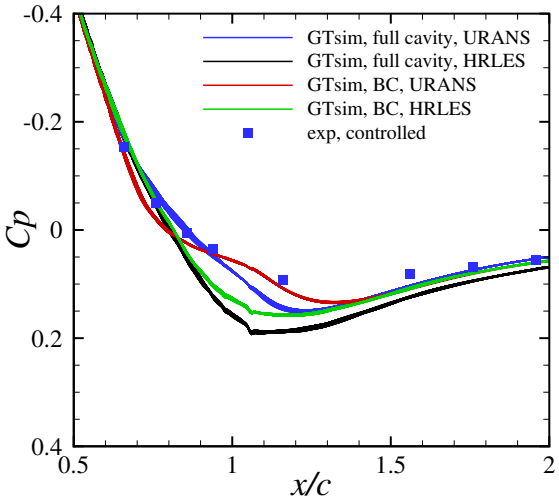

(b) Close view

Fig. 20: Controlled flow time-averaged pressure coefficient distribution over the curved surface

from pressure spikes. The differences in the pressure distributions of the four simulation approaches stem from variations in the actuator flow rates. Higher flow rates result in higher pressures at the trailing edge. The better agreement between computation and experiments with the boundary condition model and URANS appears to be serendipity, considering this approach has the highest number of approximations. Further analysis with an even more refined mesh will be examined to confirm this result for both turbulence closures. It is clear from the pressure distributions that the boundary condition model performs exceptionally well, and is therefore a valid and promising approach. This is further supported by the time-averaged flowfield.

Figures 22 and 23 provide comparisons between computation and experiments for the time-averaged vorticity and TKE respectively at the mid-plane of the test section. For HRLES, the simulation TKE is a

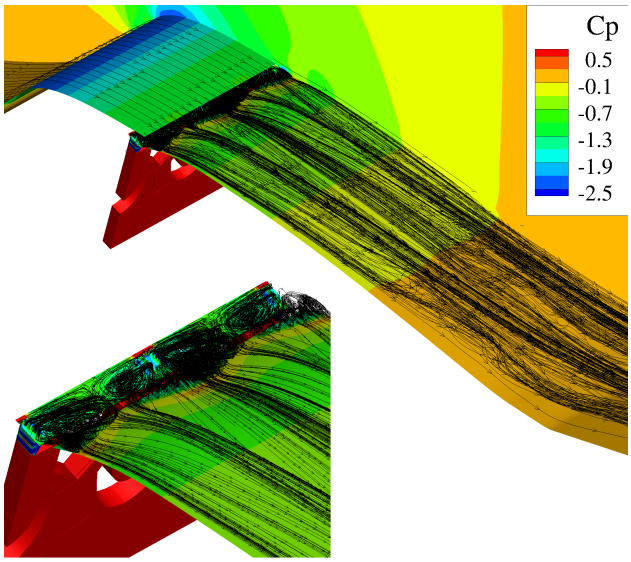

Fig. 21: Controlled flow time-averaged streamlines over the model exhibiting the vortices at the actuator exit, full cavity HRLES

summation of its modeled and resolved components. Additionally, close views of the overhang for the vorticity and TKE are provided in Fig. 24, and streamwise slices are depicted in Fig. 25 based on the HRLES simulations (full cavity and BC). Note that the contour levels are extended in Fig. 24 to show more details of the behavior at the actuator exit, and note the similarities between the results obtained with the full cavity and the boundary condition model.

The full cavity HRLES simulation provides the best agreement with experimental data for the vorticity and TKE levels. Immediately after the actuator exit and as the flow is deflected by the overhang, concentrations of vorticity and TKE are apparent in the mid-plane. This results from interactions with the outer flow, and ultimately leads to a decrease in TKE downstream, as the flow remains attached. Consistent with the large-scale structures observed in the instantaneous flowfield between the sweeping jets(Fig. 19), the streamwise slices (Fig. 25) exhibit two tubes of vorticity and TKE concentrations with and without the boundary condition model. These tubes eventually merge downstream, indicating spanwise mixing between the jets and the outer flow. These stripes of vorticity concentration and spanwise mixing downstream are consistent with experimental data reported by other researchers for a flat plate[33] or a hinged flap[34]. These findings will be confirmed for the present experimental setup via measurements in multiple spanwise planes.

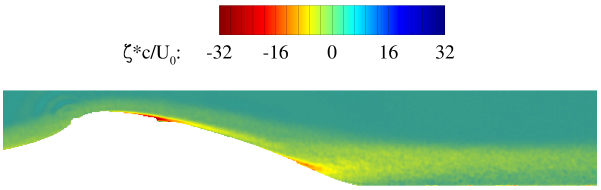

(a) Experimental results

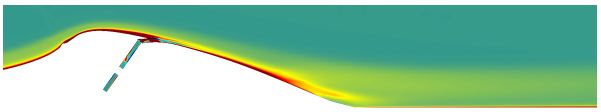

(b) Present simulation, full cavity URANS

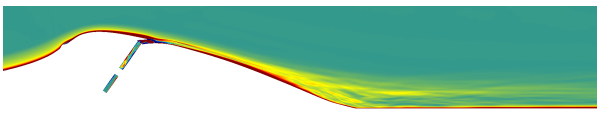

(c) Present simulation, full cavity HRLES

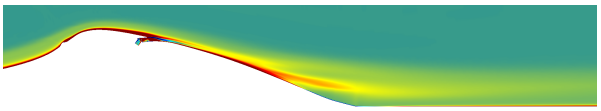

(d) Present simulation, BC URANS

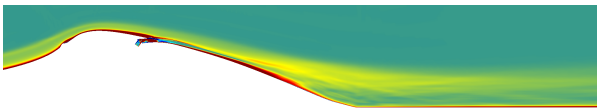

(e) Present simulation, BC HRLES

Fig. 22: Controlled flow mean out-of-plane vorticity contours

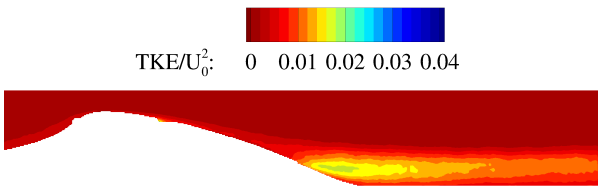

(a) Experimental results

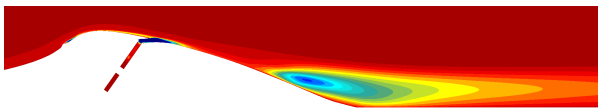

(b) Present simulation, full cavity URANS

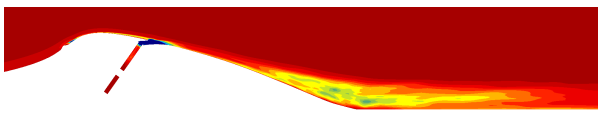

(c) Present simulation, full cavity HRLES

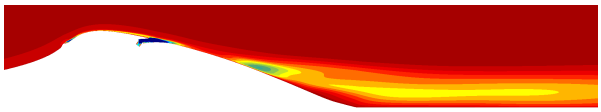

(d) Present simulation, BC URANS

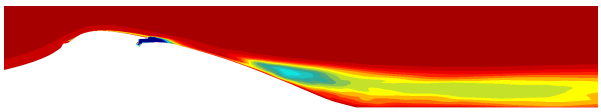

(e) Present simulation, BC HRLES

Fig. 23: Controlled flow mean in-plane TKE ($\overline{(u'^2+w'^2}/2$) contours

6 CONCLUSIONS

Results of an ongoing, joint experimental and computational study of active flow control via fluidic oscillators were presented. The results include the characterization of the isolated actuators, as well as their effect on a nominally separated flow over a rotorcraft-suitable curved surface. The following conclusions can be drawn:

- The base (un-actuated) flow over the curved surface separates at approximately 25% chord. The agreement (approximately 10% error) between experiment and simulation is satisfactory, considering the uncertainties in trip wire shape and in the absence of detailed experimental characterization of the incoming boundary layer.
- The simulation of the isolated sweeping jet actuator in quiescent conditions resulted in a characterization of its oscillation frequency. Discrepancies between computation and experiments were found for the oscillation frequency and were attributed to unaccounted pressure losses. Further investigations are warranted to elucidate these differences.
- Consistent with the experiments, the simulated oscillation frequency of an isolated fluidic oscillator was found to be unaffected by the presence of a second actuator. This indicates that the external interaction of the neighboring sweeping jets does not affect the internal mechanisms generating them. The external interaction between the jets in quiescent conditions consists in their merging downstream.
- Flow separation was entirely suppressed in a time-averaged sense, for the actuation intensity studied ($C_\mu \times 10^3 = 2.1$), in both experiments and computations.
- The URANS approach does well in predicting the pressure coefficient distribution over the model and capturing the largest flow structures for the controlled case evaluated. As expected, the HRLES approach is able to capture more of the resulting flow structures downstream.
- A boundary condition was derived from the simulation of the isolated actuator. It consists in a phase-averaged representation of the flow variables at the actuator's throat, including the modeled turbulence. Such a boundary condition performs well compared to the full cavity simulation and the experimental data.

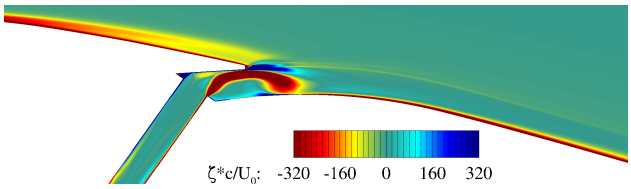

(a) Vorticity contours, full cavity HRLES

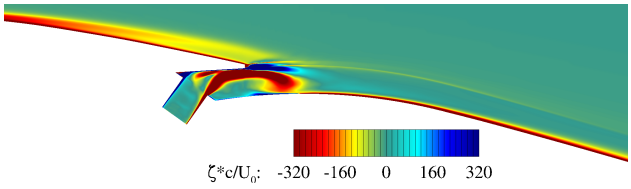

(b) Vorticity contours, BC HRLES

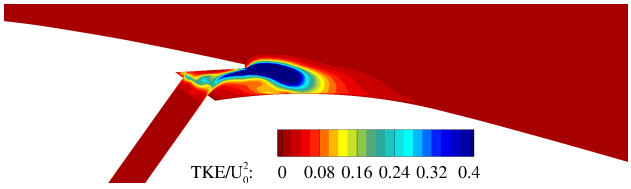

(c) TKE contours, full cavity HRLES

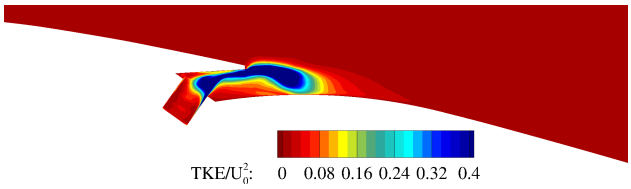

(d) TKE contours, BC HRLES

Fig. 24: Controlled flow time-averaged out-of plane vorticity and in-plane TKE ($\overline{u'^2 + w'^2}/2$) contours, close view of the overhang

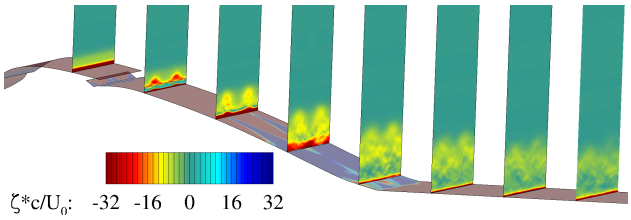

(a) Vorticity contours, full cavity HRLES

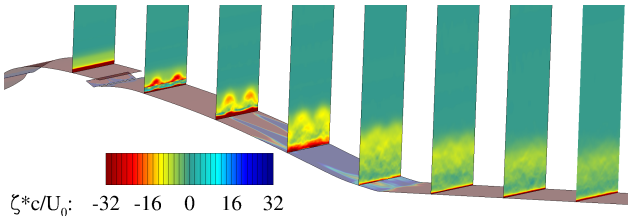

(b) Vorticity contours, BC HRLES

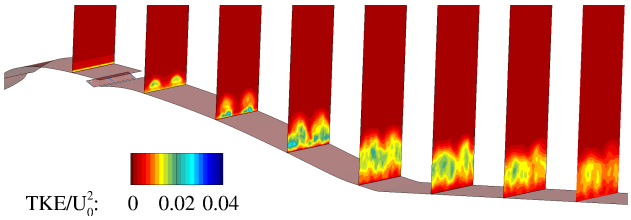

(c) TKE contours, full cavity HRLES

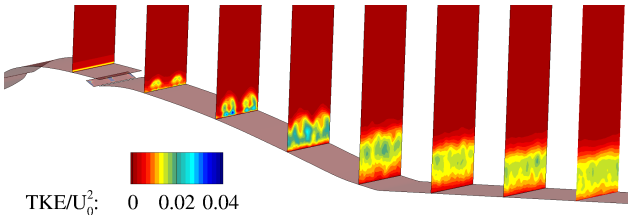

(d) TKE contours, BC HRLES

Fig. 25: Controlled flow time-averaged vorticity out of the x-z plane and TKE in the x-z plane ($\overline{u'^2 + w'^2}/2$) at different streamwise planes ($x/c =$ 0.2, 0.4, 0.6, 0.8, 1.0, 1.2, 1.4, 1.6)

FUTURE WORK

A few results presented herein merit further investigation. In particular, the correlation between computational and experimental oscillation frequency is not satisfactory yet, and the uncertainties in the experimental setup have yet to be ascertained. The differences were attributed to potential pressure losses between the pressure measurement location and the inlet of the computational domain, but this must be formally verified. Future work also includes the evaluation of other actuation intensities to determine how well the computational approach performs over an entire range of conditions. Finally, further insight will be gained into the interaction of the sweeping jets with the outer flow by collecting additional experimental data by employing stereo PIV across multiple measurement planes.

ACKNOWLEDGEMENTS

The authors would like to thank Daniel Heathcote for making some of the early meshes utilized in this effort and helpful discussions.

This research was partially funded through the U.S. Army/Navy/NASA Vertical Lift Research Center of Excellence at Georgia Tech via Task 5 under the direction of Mahendra Bhagwat of ADD-A, Agreement No. W911W6-17-2-0002. Computational time was, in part, provided through the Department of Defense (DoD) high Performance Computing Modernization Program (HPCMP) from the DoD HPC Center AFRL DSRC. Roger Strawn was the S/AAA for this HPC time, and his support is gratefully acknowledged.

COPYRIGHT STATEMENT

REFERENCES

[1] Wagner, S. N., "Problems of Estimating the Drag of a Helicopter," AGARD Conference Proceedings No. 124, Neuilly Sur Seine, France, April 1973.

[2] Seele, R., Tewes, P., Woszidlo, R., McVeigh, M. A., Lucas, N. J., and Wygnanski, I. J., "Discrete Sweeping Jets as Tools for Improving the Performance of the V-22," *Journal of Aircraft*, Vol. 46, (6), 2009, pp. 2098–2106.

[3] Wilson, J., Schatzman, D., Arad, E., Seifert, A., and Shtendel, T., "Suction and Pulsed-Blowing Flow Control Applied to an Axisymmetric Body," *AIAA Journal*, Vol. 51, (10), 2013, pp. 2432–2446.

[4] Pack Melton, L. G. and Koklu, M., "Active Flow Control Using Sweeping Jet Actuators on a Semi-Span Wing Model," AIAA 2016-1817, 54th AIAA Aerospace Sciences Meeting, San Diego, CA, January 2016.

[5] Martin, P. B., Overmeyer, A. D., Tanner, P. E., Wilson, J. S., and Jenkins, L. N., "Helicopter Fuselage Active Flow Control in the Presence of a Rotor," AHS 2014-002, Proceedings of the 70th American Helicopter Society Forum, Montréal, Canada, May 2014.

[6] Yadlin, Y., Shmilovich, A., and P. Narducci, R., "Application of Active Flow Control for Download Alleviation in Rotorcraft," AIAA 2017-3045, 2017 AIAA Aviation Forum, Denver, CO, June 2017.

[7] Otto, C., Tewes, P., Little, J. C., and Woszidlo, R., "Comparison of Fluidic Oscillators and Steady Jets for Separation Control on a Wall-Mounted Hump," AIAA 2018-1281, 2018 AIAA Aerospace Sciences Meeting, Kissimmee, FL, January 2018.

[8] Aram, S. and DeJong, A., "Numerical Comparison Between Steady and Sweeping Jets for Active Flow Control Applications," ASME Fluids Engineering Division Summer Meeting, Montreal, QC, July 2018.

[9] Woszidlo, R., Ostermann, F., and Schmidt, H.-J., "Fundamental Properties of Fluidic Oscillators for Flow Control Applications," *AIAA Journal*, Vol. 57, (3), 2019, pp. 978–992.

[10] Raghu, S., "Fluidic Oscillators for Flow Control," *Experiments in Fluids*, Vol. 54, (2), January 2013, pp. 1455.

[11] Cattafesta, L. N. and Sheplak, M., "Actuators for Active Flow Control," *Annual Review of Fluid Mechanics*, Vol. 43, (1), 2011, pp. 247–272.

[12] Gregory, J. and Tomac, M. N., "A Review of Fluidic Oscillator Development," AIAA 2013-2474, 43rd AIAA Fluid Dynamics Conference, San Diego, CA, June 2013.

[13] Shmilovich, A. and Vatsa, V. N., "Practical Computational Methods for Airplanes with Flow-Control Systems," *AIAA Journal*, Vol. 57, (1), 2019, pp. 35–52.

[14] Childs, R. E., Stremel, P. M., Garcia, J. A., Heineck, J. T., Kushner, L. K., and Storms, B. L., "Simulation of Sweep-Jet Flow Control, Single Jet and Full Vertical Tail," AIAA 2016-0569, 54th AIAA Aerospace Sciences Meeting, San Diego, CA, January 2016.

[15] Aram, S., Lee, Y.-T., Shan, H., and Vargas, A., "Computational Fluid Dynamic Analysis of Fluidic Actuator for Active Flow Control Applications," *AIAA Journal*, Vol. 56, (1), January 2018, pp. 111–120.

[16] Koukpaizan, N. K., Heathcote, D. J., Glezer, A., and Smith, M. J., "Numerical Simulation of Fluidic Oscillators for Flow Control," AHS 2019-050, Proceedings of the 75th Annual VFS Forum and Technology Display, Philadelphia, PA, May 13–16 2019.

[17] Vatsa, V. N., Duda, B., Fares, E., and Lin, J., "Numerical Simulation of a High-Lift Configuration Embedded with High Momentum Fluidic Actuators," AIAA 2016-3932, 8th AIAA Flow Control Conference, Washington, D.C., June 2016.

[18] Shmilovich, A. and Yadlin, Y., "Active Flow Control Computations: From a Single Actuator to a Complete Airplane," *AIAA Journal*, Vol. 56, (12), 2018, pp. 4730–4740.

[19] Aram, S. and Shan, H., "Synchronization Effect of an Array of Sweeping Jets on a Separated Flow over a Wall-Mounted Hump," AIAA 2019-3396, 2019 AIAA Aviation Forum, Dallas, TX, June 2019.

[20] Tomac, M. N. and Gregory, J. W., "Oscillation Characteristics of Mutually Impinging Dual Jets in a Mixing Chamber," *Physics of fluids*, Vol. 30, (11), 2018, pp. 117102.

[21] Peterson, C., Vukasinovic, B., Smith, M. J., and Glezer, A., "Control of a Closed Separation Domain in Adverse Pressure Gradient Over a Curved Surface," AIAA 2019-1900, 57th AIAA Aerospace Sciences Meeting, San Diego, CA, January 2019.

[22] Hodara, J., *Hybrid RANS-LES Closure for Separated Flows in the Transitional Regime*, Ph.D. thesis, Georgia Institute of Technology, Atlanta, GA, hdl.handle.net/1853/54995, May 2016.

[23] Langtry, R. B. and Menter, F. R., "Correlation-Based Transition Modeling for Unstructured Parallelized Computational Fluid Dynamics Codes," *AIAA Journal*, Vol. 47, (12), 2009, pp. 2894–2906.

[24] Hodara, J. and Smith, M. J., "Hybrid Reynolds-Averaged Navier-Stokes/Large-Eddy Simulation Closure for Separated Transitional Flows," *AIAA Journal*, Vol. 55, 2017, pp. 1948–1958.

[25] Menter, F. R., Kuntz, M., and Langtry, R., "Ten Years of Industrial Experience with the SST Turbulence Model," *Turbulence, Heat and Mass Transfer*, Vol. 4, (1), 2003, pp. 625–632.

[26] Sánchez-Rocha, M., Kirtas, M., and Menon, S., "Zonal Hybrid RANS-LES Method for Static and Oscillating Airfoils and Wings," AIAA 2006-1256, 44th AIAA Aerospace Sciences Meeting, Reno, NV, January 2006.

[27] Kim, W.-W. and Menon, S., "An Unsteady Incompressible Navier–Stokes Solver for Large Eddy Simulation of Turbulent Flows," *International Journal for Numerical Methods in Fluids*, Vol. 31, (6), 1999, pp. 983–1017.

[28] Roe, P., "Characteristic-Based Schemes for the Euler Equations," *Annual Review of Fluid Mechanics*, Vol. 18, (1), 1986, pp. 337–365.

[29] Borges, R., Carmona, M., Costa, B., and Don, W. S., "An Improved Weighted Essentially Non-Oscillatory Scheme for Hyperbolic Conservation Laws," *Journal of Computational Physics*, Vol. 227, (6), 2008, pp. 3191 – 3211.

[30] Ducros, F., Laporte, F., Soulres, T., Guinot, V., Moinat, P., and Caruelle, B., "High-Order Fluxes for Conservative Skew-Symmetric-like Schemes in Structured Meshes: Application to Compressible Flows," *Journal of Computational Physics*, Vol. 161, (1), 2000, pp. 114 – 139.

[31] Titarev, V. and Toro, E., "Finite-Volume WENO Schemes for Three-Dimensional Conservation Laws," *Journal of Computational Physics*, Vol. 201, (1), 2004, pp. 238 – 260.

[32] Hirsch, D. and Gharib, M., "Schlieren Visualization and Analysis of Sweeping Jet Actuator Dynamics," *AIAA Journal*, Vol. 56, (8), 2018, pp. 2947–2960.

[33] Wilson, J., Schatzman, D. M., Seifert, A., Arad, E., Marom, L., Shay, N., and Palei, V., "Characterization of SaOB Actuators Interacting With Flat Plate Boundary Layers," 55th AIAA Aerospace Sciences Meeting, Grapevine, TX, January 2017.

[34] Melton, L. P., Koklu, M., Andino, M., and Lin, J. C., "Active Flow Control via Discrete Sweeping and Steady Jets on a Simple-Hinged Flap," *AIAA Journal*, Vol. 56, (8), 2018, pp. 2961–2973.